Details on Hysteretic Property Measurements [Ivanov99]

Hysteretic parameters were measured using a Magniscope, an instrument designed and used in the Metals Development Lab at Iowa State University. This instrument allows "local" measurement of the B-H characteristics for ferromagnetic materials. The B-H curve is measured by magnetizing a small volume of the sample, using a yoke. The field intensity is measured, with a Hall probe located in the middle of the yoke. The probe is oriented to pick up the horizontal component of the field. The flux density is measured using a coil wound on the yoke. Parameters such as coercivity, remanence, and hysteresis loss are estimated from the **6-H** curve. The depth of measurement is roughly equivalent to half the distance between the poles of the yoke. **A** half-inch probe was used; the penetration depth was, therefore, approximately 0.25 inch.

Measurements were made on the surface opposite the defect. The scanning area was 3 by 3 inches, divided into a 12 by 12 grid, with the defect located in the middle of the scanned area. The measurement procedure included demagnetization, registration of a single hysteresis loop, and demagnetization again. Care was taken so that the orientation of the magnetic field remained constant. Measurements were taken with the field oriented in two perpendicular directions. Measurements were also made on a circular grid with eight divisions along the circumference and six divisions along the radius, resulting in **48** measurement locations. The magnetization field for circular measurement was radially oriented. This was done in order to maintain the symmetry of the residual stress field.

The resulting sets of data were processed and are shown below. The data were compared with the stress distribution patterns obtained from the structural finite-element model discussed earlier. For example, the scan shown in the first figure represents the distribution of coercivity (H) around a defect corresponding to a 30 kip load. The second figure shows the calculated residual stresses for the same defect.

The small variation of coercivity around the metal-loss defect in the first figure is a result of measurement and instrumentation error and does not indicate a variation of the coercivity of the material. No variation should be expected because the area is free of stress. The pattern around the pressed-in gouge exhibits a very large variation, on the order of 25 percent. This variation represents the residual stress in the sample due to the mechanical damage. The third and fourth figures show the distribution of remanence and hysteresis **loss** around the same defect. Similar results are observed.

The results suggest that the residual stress can be linked to magnetic parameters, such as coercivity, remanence, and hysteresis loss. **All** of the circular scans showed patterns of the shape similar to the expected stress distribution in the test samples. The sensitivity of a parameter to residual stress can be estimated from the relative change in the observed pattern. Remanence is more sensitive than coercivity, but hysteresis loss was most sensitive.

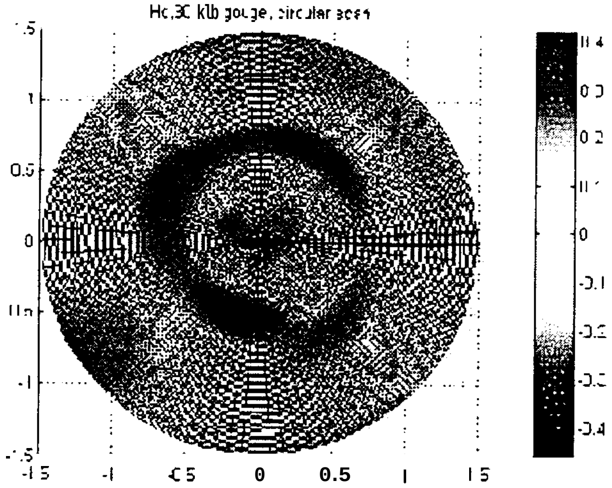

Coercivity distribution

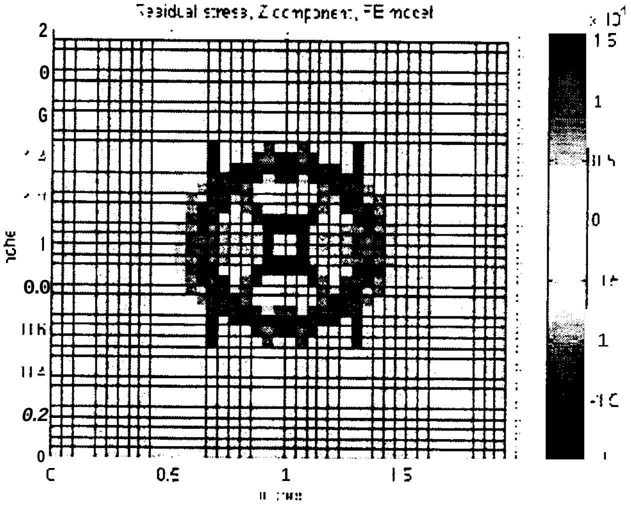

Residual stress distribution

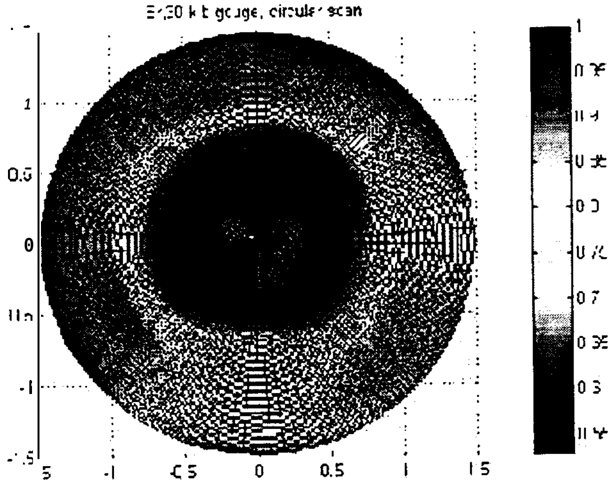

Remanence distribution

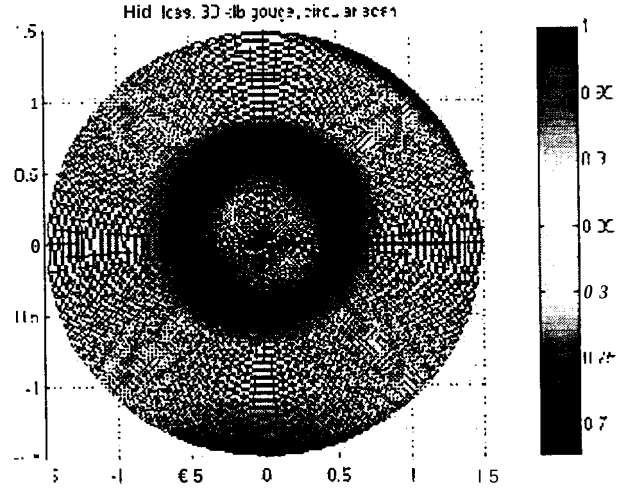

Hysteresis loss distribution

Additional Details on Defect Characterization[Hwang96, Hwang97]

Both radial basis and wavelet functions were used to perform three-dimensional defect characterization from the MFL signals. These networks were used to predict the shape of the defect (either corrosion or mechanical damage) using input parameters taken from the MFL signals. Typically, the MFL signal was transformed, for example, by converting the signal to its equivalent components in the frequency domain, after which 6 to 10 features from the transformed signal were chosen as input.

The radial basis function networks were developed under an earlier project for GRI. The wavelet network architecture is similar to that of the radial basis network, however, it uses wavelets for functional approximation. Wavelets can be expressed using

$$F = \sum_{k=1}^{n_L} c_k^L \phi\left(\left\| x - c_{\phi_k} \right\|\right) + \sum_{m=1}^{L} \sum_{k=1}^{n_m} d_k^m \psi\left(\left\| x - c_{\psi_k^m} \right\|\right)$$

where c_ϕ and c_ψ are known as the "centers" of the wavelet network, ϕ and ψ denote scaling wavelet functions, and c_k and d_k specify wavelet transform coefficients. The use of wavelets as basis functions provides a simplified training procedure and a trade-off between computational complexity and prediction accuracy in defect characterization.

A Gaussian radial basis function was used for scaling, and the Mexican hat wavelet, which is related to the second derivative of a Gaussian, was used as the wavelet function. The basis function width (one of the parameters describing the function) at the finest resolution was chosen in order to cover the full range of input parameters. The unknown weights were calculated using a matrix inversion technique.

Defect Characterization Using Feedback Neural Networks

Existing defect characterization schemes are usually incapable of providing an outline measure of the accuracy of their prediction results. This section describes a novel method for characterizing defects that overcomes this deficiency. The method is based on solving the inverse problem (i.e., estimating the defect profile based on information contained in a measured signal) using a feedback system.

Solution techniques for inverse problems can be divided into two broad categories: phenomenological and non-phenomenological. Phenomenological approaches typically employ a forward model that simulates the underlying physical process to solve the inverse problem; examples of forward models include finite-element and finite-difference methods. Non-phenomenological typically use signal processing techniques.

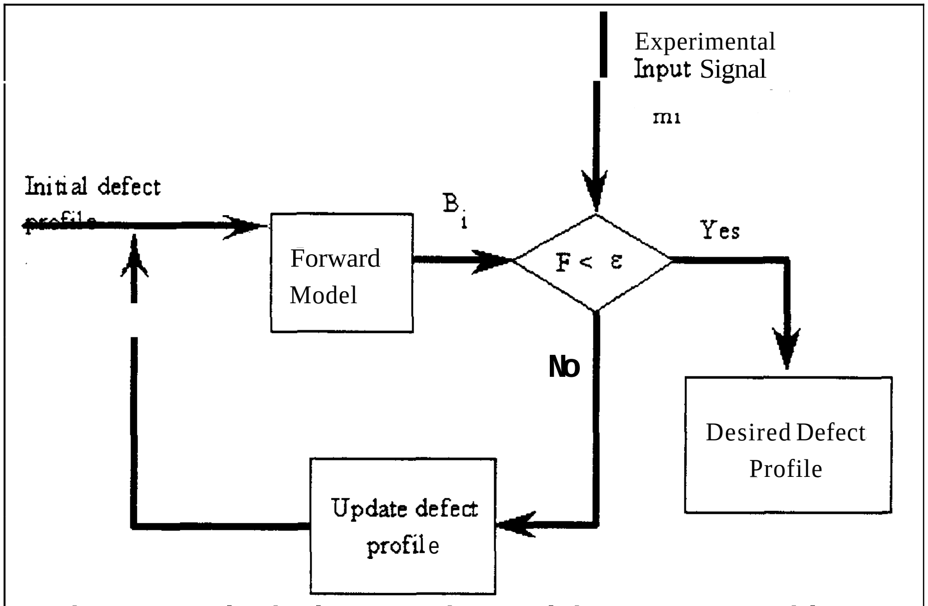

Phenomenological Approach to Solving Inverse Problems

When a phenomenological model is used in a feedback configuration (shown at right), an initial estimate of the defect profile is input into the forward model. The output of the model is the theoretical signal corresponding to the estimated defect profile. This signal is then compared to an experimentally measured signal. If the prediction error is less than some preset threshold, the initial solution is assumed to be the desired defect profile. On the other hand, a higher error indicates the need for further refinement of the solution (defect profile). This process is carried out in an iterative manner until a satisfactory solution is reached. Feedback systems are inherently less sensitive to noise, and therefore, likely to offer more accurate results.

The second class of approaches, which is non-phenomenological in nature, attempts to solve the inverse problem using signal processing techniques. Typical approaches include calibration methods and neural-networks-based techniques. In the case of the latter, the problem is formulated as a *function-approximation problem* and the underlying function mapping is "learned" by a neural network.

Methods utilizing these approaches have been reported extensively in the literature.[Yan97, Hoole91, Hwang97] However, these methods have certain drawbacks. Neural-network-based techniques are open loop in nature and are capable of providing confidence measures relating to accuracy only during the training phase.

A novel method of solving the inverse problem was developed in this project The following links describe the alternative method for characterizing defects, which incorporates the strengths of both phenomenological and non-phenomenological techniques. The technique is capable of incremental learning, provides an online measure for accuracy of the defect estimate, and is computationally efficient.

- Feedback neural network scheme for defect
- Initial results of applying the algorithm to MFL signals

Feedback Neural Network Approach

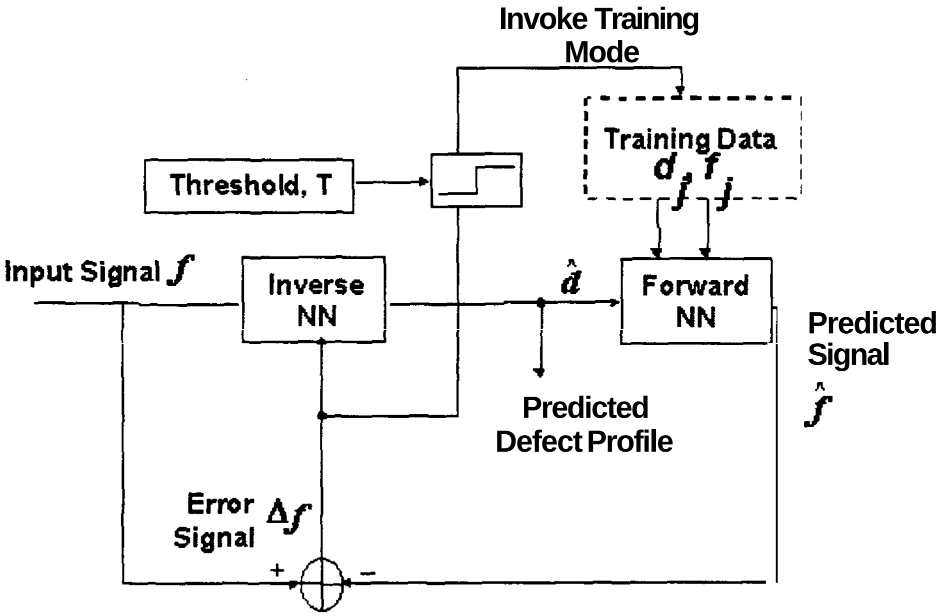

Schematic of Feedback Neural Network Approach (Prediction Mode)

Inverse problems in nondestructive evaluations involve the estimation of defect profiles in materials. Estimating defect profiles can be formulated as a function-approximation problem and the solution obtained using artificial neural networks. In order to retain the advantages of phenomenological and non-phenomenological solution techniques, and to overcome the disadvantages of phenomenological methods, a feedback neural network scheme was developed for solving the inverse problem.

The feedback neural network approach is shown at right. Two neural networks are used in a feedback configuration. The forward network predicts the signal corresponding to a defect profile while the inverse network predicts a profile given an inspection signal. The forward network provides a reference for comparing the defect profile predicted by the inverse neural network.

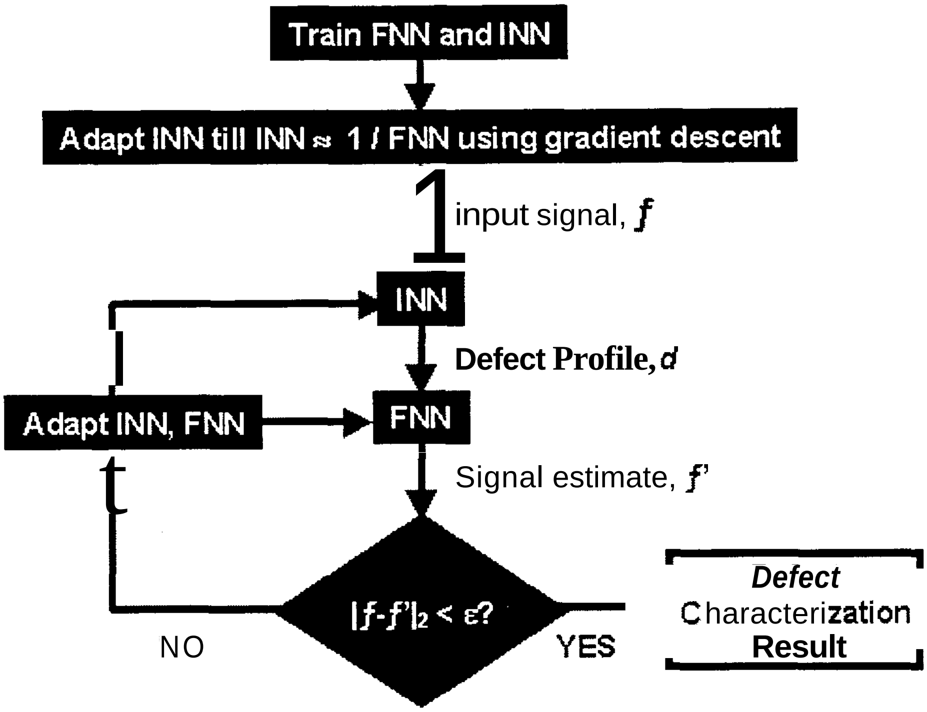

Feedback Neural Network Algorithm

Approach to Solving the Inverse Problem

The overall approach to solving the inverse problem is shown here. The input signal, f, from a defect of unknown profile is input to the characterization neural network (inverse neural network or INN) to obtain an estimate of the profile This estimate is then input into the forward neural network (FNN) to get the corresponding prediction of the MFL signal for that estimate of the profile. If the estimated defect profile is close to the true profile, the measured MFL signal and the predicted **signal** from the forward network will be similar to each other. This is the basis of the feedback neural network scheme.

The following links provide details on the forward network, the inverse network, and the methodology used to optimize the network system:

The Forward Network
The Inverse Network
Optimization

Forward Network

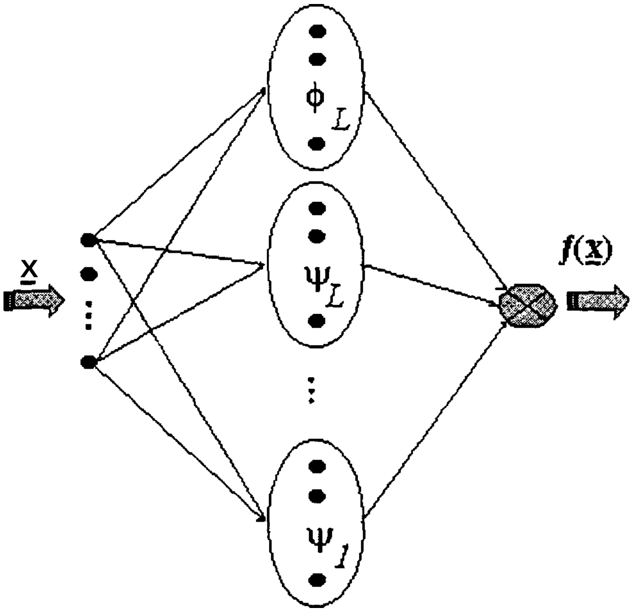

Wavelet Basis Function Neural Network

Since the forward neural network serves as a "standard' for measuring the performance of the feedback neural network scheme, it must be capable of accurately estimating the signal obtained from a variety of defect profiles. A wavelet basis function neural network is used for implementing the forward network. The structure of a wavelet basis function network is shown at right. The wavelet basis function neural network uses a multi-resolution function approximation.[Hwang97] **given by**

$$f = \sum_{k=1}^{N_L} s_k^L \phi_k^L + \sum_{j=1}^{L} \sum_{k=l}^{N_j} d_k^j \psi_k^j$$

The networks use a single hidden layer with sets of function nodes depending on the number of resolutions. A family of wavelets is used as the basis functions and the network is fully interconnected. Training of wavelet basis function neural networks involves determining the weights connecting the hidden layer nodes to the output layer nodes as well as the centers and spreads of the basis functions. Centers of the scaling functions at the coarse (or first) resolution are determined by using a K-means clustering algorithm while the centers of the wavelet functions at higher (or finer) resolutions are computed using a dyadic grid. The spreads of these functions are set proportional to the cluster sizes. The interconnection weights are then computed using a matrix inversion step. The network used in this study employs Mexican hat functions as the wavelet and a Gaussian function is employed as the scaling function.

On to information on the Inverse Network.

Inverse Network

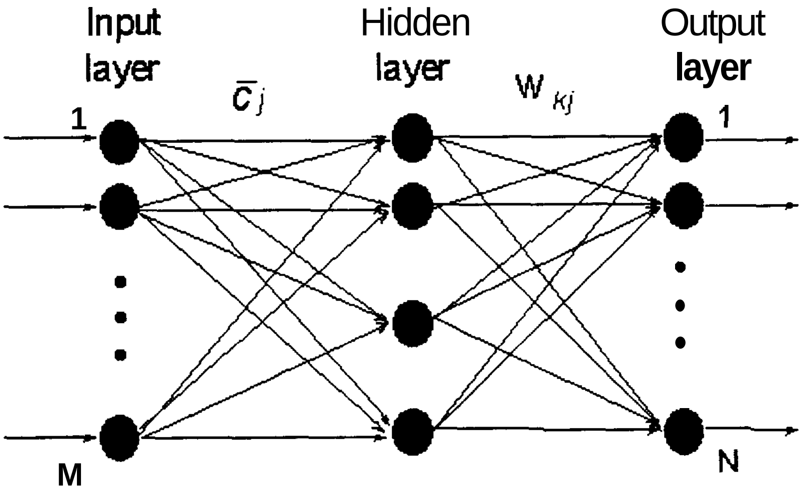

Radial Basis Function Neural Network

The Inverse Network

A radial basis function neural network is used as an inverse network for characterizing the defect profiles. The radial basis function is a three-layer function approximation network, as shown at right. The structure of the network is similar to that of a wavelet basis function neural network. The difference lies in the fact that the radial basis function uses a single set of basis functions (the scaling functions in the wavelet basis function neural network). The training algorithm for the radial basis function is similar to that of the wavelet basis function neural network with the centers of the basis functions determined by using a clustering algorithm. The spread of each basis function is proportional to the cluster size. Alternatively, it may be set to some common constant value for all bases. The output interconnection weights are then determined by a matrix inversion step.

On to information on optimization of the networks.

Optimization

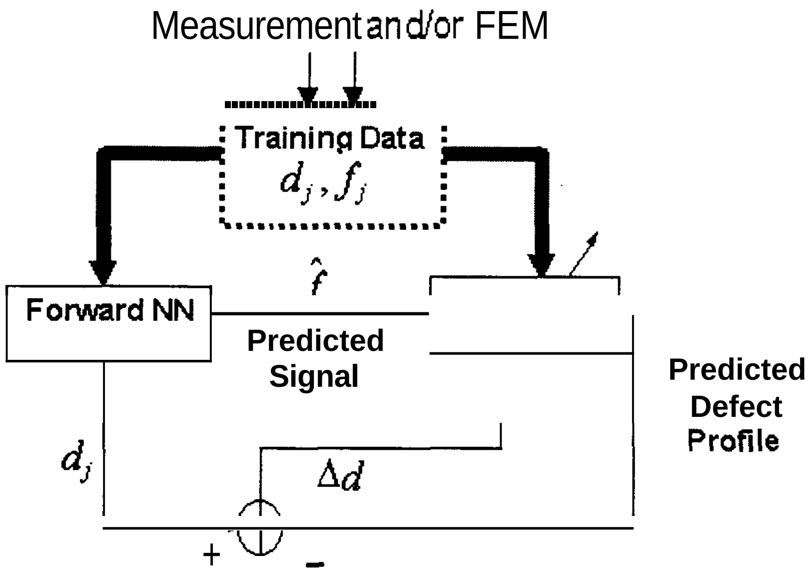

Feedback Neural Network Training Mode

Optimization

Once the inverse network is trained, the parameters need to be optimized. This process is referred to as the training mode. The goal of the optimization procedure is to minimize the error due to the inverse radial basis function network. Let *Df* be the error between the actual MFL signal and the prediction of the forward network in the feedback configuration. In order for Df to be zero, the characterization network must be an exact inverse of the forward network. While the functional form of the forward network can be derived easily, obtaining its inverse analytically is difficult. This is because the output of the forward network is a function of the number and location of their respective basis function centers in each network. The inverse is, therefore, estimated numerically.

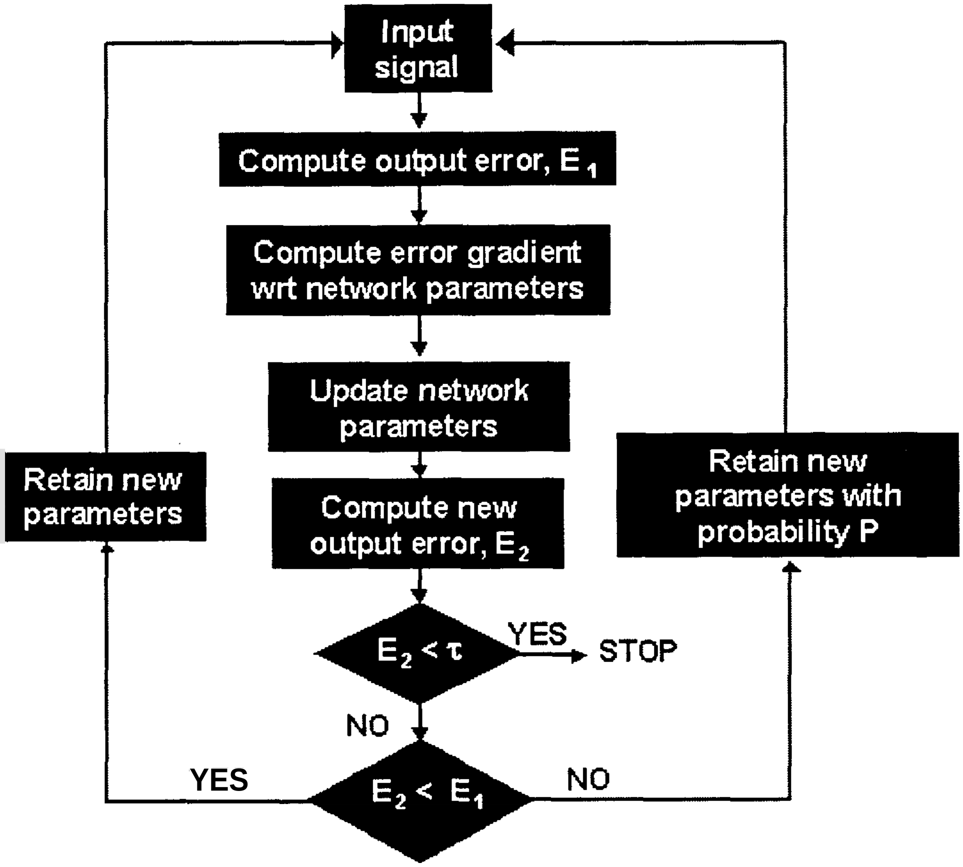

Inverse Neural Network Optimization

An adaptive scheme is used to estimate the inverse of the forward network as shown above. This "inverse network" is used as the characterization network. The algorithm uses gradient descent in combination with simulated annealing to optimize the inverse network parameters. The algorithm is shown at right, and the derivation of the network parameter update equations is shown below. As shown in the flowchart, the defect profile is input to the forward network. The output of the forward network (the predicted signal) is input to the inverse network. The defect profile predicted by the inverse network is compared to the true profile and the error is used to update the inverse network parameters. This occurs only if the error after the update is less than the error before the update. In case the error increases, the update is retained with a probability ***p*** that decreases as the number of iterations increases. This probabilistic update rule is used to escape from local minima, which the gradient descent rule is susceptible to get trapped in.

Let E = the error at the output of the inverse network,

w_{kj} = interconnection weight from node j in the hidden layer to node **k** in the output layer

$\mathbf{c}_j$ = center of the j^{th} basis function (at node j in the hidden layer)

s_j = spread of the jth basis function

f = the signal

$\mathbf{d} = (d_1, d_2, \ldots, d_k, \ldots d_n)$ be the desired output of the radial basis function network

$\hat{\mathbf{d}} = (\hat{d}_1, \hat{d}_2, \ldots, \hat{d}_k, \ldots \hat{d}_n)$ be the actual output of the radial basis function network

Then, the error E can be defined as

$$E = \sum_{k=1}^{N} \left(d_k - \hat{d}_k\right)$$

where d_k is given by

$$\hat{d}_k = \sum_{j=1}^{I} w_{kj} \phi\left(\frac{\|\mathbf{f} - \mathbf{c}_j\|}{2\sigma_j^2}\right)$$

and the basis function is chosen to be a Gaussian function:

$$\phi\left(\frac{\|\mathbf{f} - \mathbf{c}_j\|}{2\sigma_j^2}\right) = \exp\left(-\frac{\|\mathbf{f} - \mathbf{c}_j\|^2}{2\sigma_j^2}\right)$$

Substituting the second two equations into the first equation and taking the derivative with respect to the weights w_{kj}, we have

$$\frac{\partial E}{\partial w_{kj}} = -2\left(d_k - \hat{d}_k\right) \phi\left(\frac{\|\mathbf{f} - \mathbf{c}_j\|}{2\sigma_j^2}\right)$$

Similarly, the derivative of the error with respect to the other two parameters (c_j and s_j) can be computed as follows:

$$\frac{\partial E}{\partial c_{ji}} = \sum_{k=1}^{n} -2\left(d_k - \hat{d}_k\right)\left[w_{kj} \phi\left(\frac{\|\mathbf{f} - \mathbf{c}_j\|}{2\sigma_j^2}\right)\left(\frac{f_i - c_{ji}}{\sigma_j^2}\right)\right]$$

$$\frac{\partial E}{\partial \sigma_j} = \sum_{k=1}^{n} -2\left(d_k - \hat{d}_k\right)\left[w_{kj}\phi\left(\frac{\|\mathbf{f}-\mathbf{c}_j\|}{2\sigma_j^2}\right)\left(\frac{\|\mathbf{f}-\mathbf{c}_j\|^2}{\sigma_j^3}\right)\right]$$

The derivatives are then substituted into the gradient descent equation to derive the update equations for the three parameters. These expressions are given by the following equations.

$$w_{kj}^{new} = w_{kj}^{old} + \eta\left(-\frac{\partial E}{\partial w_{kj}}\right)$$

$$c_{ji}^{new} = c_{ji}^{old} + \eta\left(-\frac{\partial E}{\partial c_{ji}}\right)$$

$$\sigma_j^{new} = \sigma_j^{old} + \eta\left(-\frac{\partial E}{\partial \sigma_j}\right)$$

Once the characterization network is trained and optimized, the two networks are connected in the feedback configuration shown earlier. The characterization network can then be used for predicting flaw profiles using signals obtained from defects of unknown shape and size.

Back to information on feedback neural network approach.

Initial Results of Applying the Feedback Neural Network Algorithm to MFL Signals

Testing

The feedback neural network algorithm developed in this program was tested with calculated MFL data. The data were generated using a two-dimensional finite-element model having a 100x100-element mesh. A wavelet basis function neural network was used as the forward network, while a radial basis function network was used as the inverse network for characterization. The wavelet basis function network used three resolution levels with six centers at the coarsest resolution, with the centers at other resolutions computed using a dyadic grid. The radial basis function used 150 basis functions in its hidden layer.

A total of 218 pairs of defect profiles and MFL signals were used in the training set, and 22 signals were used for testing. There was no overlap between the two data sets. The entire data set included defect widths from 1" to 7" with 0.4" increments. At each width, fifteen different depths (from 15% deep to 85% deep at 5% increments) were included. The 22 test signals were picked at random out of these defects and were not included in the training database.

Results

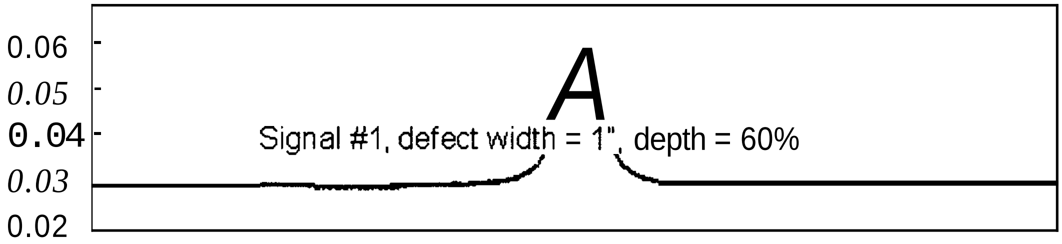

The above figure shows typical results of training the forward network (clicking on the figure will display more results). The solid line shows the true signal while the dotted line shows the neural network prediction. These plots indicate that the forward network is capable of predicting the signal with little error.

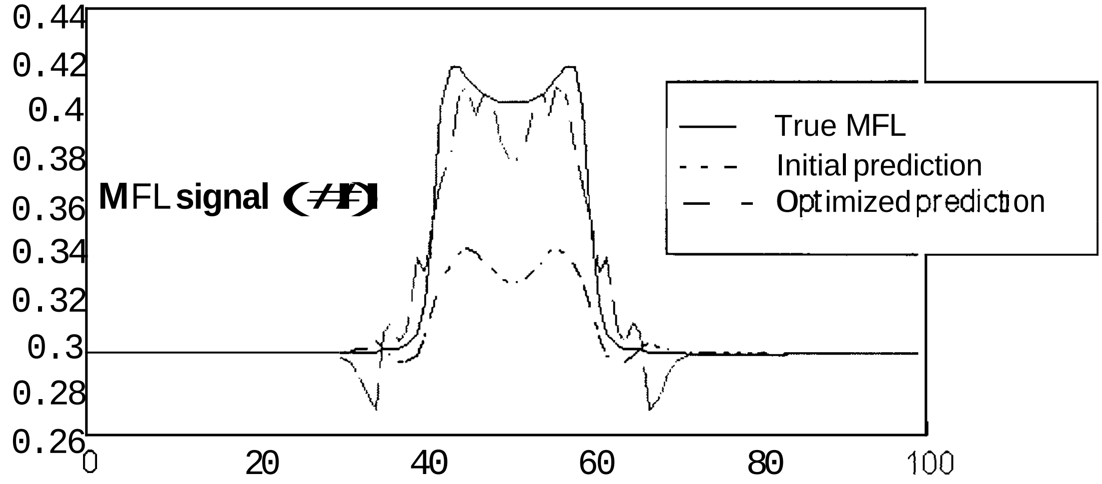

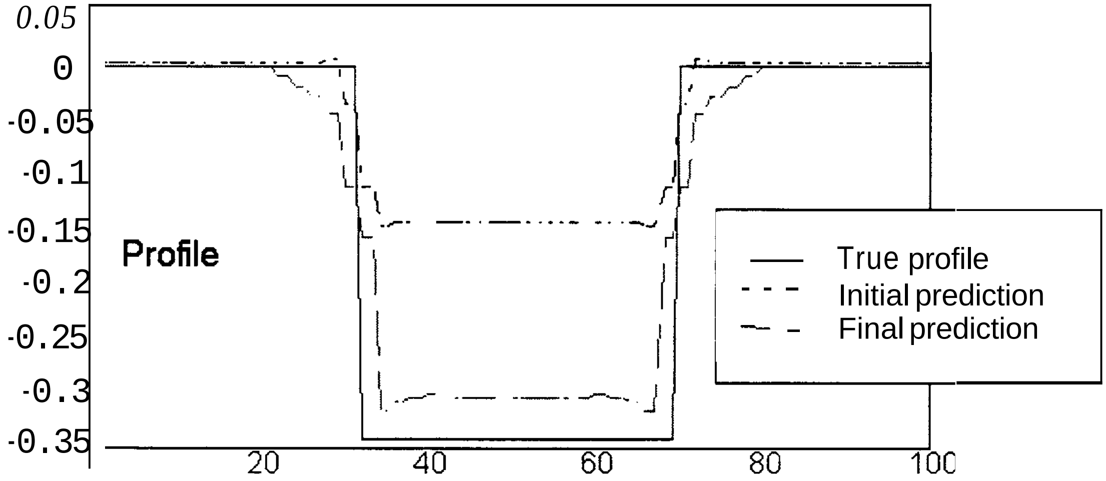

A typical prediction result is shown above. In the top figure, the solid blue line shows the true signal. This is the initial signal that is used as input into the radial basis function network, which has not been optimized. The initial prediction using the true signal is input is shown as the black dot-dash line in the lower figure. The initial prediction is then input to the forward network. Its output is shown as the black dot-dash line in the upper figure.

Results obtained after optimization of the inverse network are also shown as the red dashed lines. Similar results obtained by analyzing signals from defects of other geometries are shown for Signal #13 and Signal #14.

These results indicate that the optimization process improves the prediction results. In addition, the use of a forward network in a feedback configuration provides a measure of the error in the characterization: the error in the defect profile prediction is approximately proportional to the error in the signal prediction.

Background on Stress Corrosion Cracking

Stress-corrosion cracking (SCC) results from the combined action of stress, a cracking (electrochemical) environment, and temperature to cause cracks to initiate and grow in a susceptible line-pipe steel. Individual cracks are generally oriented perpendicular to the maximum stress and parallel to the pipe axis. Groups of cracks usually occur in what is known as a "colony." In extreme cases, these colonies may be several feet long and extend nearly around the circumference.

SCC colonies are considered sparse if the cracks are far apart in the circumferential direction and dense if the cracks are circumferentially close together. Individual cracks can range from shallow to deep. Many cracks in the middle of dense colonies have a depth less than ten percent of the wall thickness. In sparse colonies and in some dense colonies, the cracks can grow in a stable manner until they reach nearly through the wall. These deeper cracks are of primary concern in inspections to evaluate pipeline integrity.

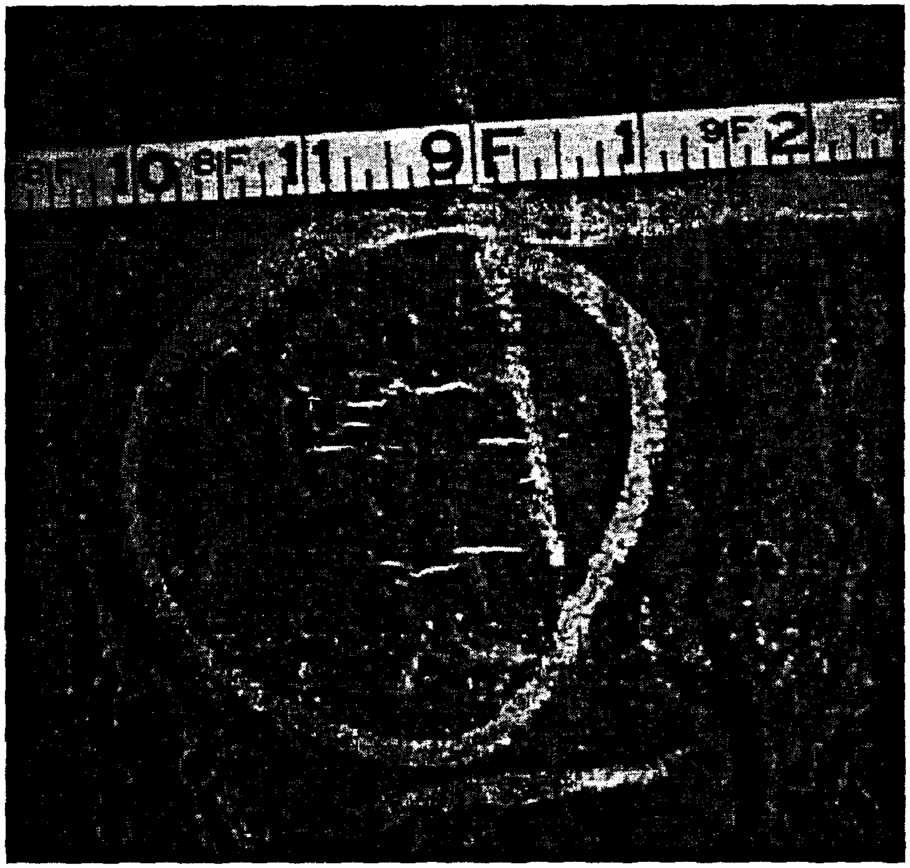

Stress Corrosion Cracking

As nearby cracks grow, individual cracks can coalescence or join to form a single, larger crack. If the coalesced crack is long enough, it can rupture. The consequences of a rupture are usually more severe than those of a leak. As a result, long deep cracks, and deep cracks that are close enough to coalesce into a crack that is long enough to rupture, are of primary concern when inspecting pipeline.

Two forms of SCC have been encountered: high pH and low pH. The surfaces of most low and high-pH stress-corrosion cracks are not smooth but irregular. High-pH stress-corrosion cracks are typically intergranular (with a cracking path along the grain boundaries of the material), with essentially little or no separation or opening between the crack faces. Low-pH cracks are often transgranular, where the fracture surfaces are smoother than intergranular fracture surfaces, but they are not as smooth as fatigue cracks. Also, both forms of cracking can branch as cracks grow through the wall thickness.

Additional Impact of Cracks on Inspection Requirements

The severity or criticality of a set of stress-corrosion cracks is most strongly a function of the length, depth, and spacing between individual cracks. Crack length and depth, along with stress level and pipe toughness, determine whether an individual crack will fracture or fail unstably. Spacing between cracks determines whether one or more cracks will coalesce before or during a failure. The nucleation and growth of stress-corrosion cracks are becoming better understood, and models for predicting crack criticality are in development. However, detailed predictions are not yet feasible. The following discussion focuses on the likelihood of near-term failure as a primary criterion for determining which cracks should be found.

Years of pipeline operating experience have demonstrated that small imperfections (for example, small regions of corrosion metal loss) cause only a small reduction in failure pressure. If the imperfections do not grow, they do not significantly threaten the integrity or serviceability of a pipeline. Consequently, in developing guidelines for acceptable corrosion loss during the 1960s and 1970s, the pipeline industry defined **a** hydrotest to the specified minimum yield (or design) strength as a fundamental requirement for pipeline safety. An acceptable imperfection was defined as one that could pass such a hydrotest. A defect was taken as one that would not survive a hydrotest of 100 percent of the pipe's yield stress.

In recent work, Battelle developed a comprehensive failure criterion for individual stress-corrosion cracks in a program sponsored by the Pipeline Research Committee. This criterion is more accurate than and represents a significant improvement over corrosion flaw severity criteria used by the pipeline industry.

Stress-corrosion cracks cannot be considered independently, though, because their ultimate failure may involve coalescence of several cracks. If two (or more) cracks coalesce, the resulting crack length increases. As a result, the coalescence of several cracks that could each survive a high-pressure hydrotest could result in a single crack that would be on the verge of failure at typical operating pressure. **As** a result, basing inspection requirements on failure at high pressure alone, without considering the likelihood of coalescence, could lead to nonconservative results if nearby cracks coalesce. Accounting for the likelihood of coalescence increases the emphasis on shorter, deep cracks in setting inspection requirements.

Details on the SLIC Systems

In the 1980s and early 1990s, Southwest Research Institute (SwRI) developed two inspection techniques to overcome problems associated with sizing near-surface axial cracks from the outside surface of a pipe. The SwRI techniques are referred to by the acronym SLIC, which stands for simultaneous use of shear and longitudinal waves to inspect and characterize flaws.

The SLIC-30 module is designed to enhance the ability of an ultrasonic examiner to estimate small crack depths. Two transducers are used, one to transmit a wave and one to receive. The first transmits a nearly perpendicular (70 degree) longitudinal (compression) beam that is directed at the crack face. This beam generates a set of longitudinal waves that are nearly parallel to the crack from both the surface and the crack tip. **A** second, low-beam (10 degree) transducer measures these secondary pulses.

The SLIC-50 system is designed to overcome shoe noise and surface reverberation that can mask the weak diffracted signals from the bottom of a shallow crack. Unlike the SLIC-30 system, the SLIC-50 system receives both longitudinal and shear waves. This feature allows the system to measure crack depth regardless of the separation between the transducer and the crack.

The SLIC-50 system operates by transmitting an interrogating wave, and then sensing a pair of associated diffracted signals (a doublet, for short) from the crack tips in the through-wall direction. **A** unique feature of the SLIC-50 system is that the distance between the doublet signals is practically independent of the position of the sensor.

General Theory of Velocity-Induced Remote Fields

Conventional pipeline inspection tools generate axially oriented magnetic fields, which are sensitive to the presence of circumferential cracks. The inspection tool is insensitive to SCC, though, because they are oriented largely in the axial direction. **A** possible alternative is to utilize the fields associated with the circumferential currents generated in the pipe wall by the movement of the magnetizer relative to the pipe wall.

The most general governing equation describing the physics underlying the motion of a pig in a pipe with a defect is:

$$\nabla \times \frac{1}{\mu} \nabla \times \vec{A} = \vec{J}_S - \sigma \frac{\partial \vec{A}}{\partial t} + \sigma \vec{V} \times \nabla \times \vec{A} \qquad (1)$$

Where the term $\sigma \frac{\partial \vec{A}}{\partial t}$ represents the defect-induced current density resulting from the time-varying magnetic field caused by the changing spatial relation between the defect and magnetizer. In the case of a defect-free pipe, this term is zero. The term $\sigma \vec{V} \times \nabla \times \vec{A}$ represents the currents induced by the velocity of the magnetizer relative to the pipe wall.

Since the motion of the tool inside the pipe is along the pipe axis, the motional electro-magnetic force due to the $\vec{V} \times \vec{B}$ term is negligible between the poles of the magnet. However, at the poles, the radially oriented magnetic fields generate a significant amount of circumferentially directed currents in the pipe. The intersection of these motion-induced currents with axial cracks results in a perturbation of the current distribution.

The fields associated with the perturbation currents carry information related to the axial cracks. In general, the fields and resulting currents are large close to the magnetizer, making the measurement of small perturbation fields difficult. So, in this work, we considered the current perturbation in the remote field region of the magnetizer.

Details on Finite-Element Modeling of Velocity-Induced Remote Fields [Yang98]

Modeling of the interaction between axial cracks and circumferential currents is a significant challenge in terms of computation time and memory requirements. The challenges arise due to nonlinearity of material properties, the size of the cracks relative to that of the magnetizer, and the time stepping involved in modeling velocity effects. The approach used here to surmount these difficulties was to decompose the overall task into three simpler subtasks that can be performed sequentially:

- Step 1: Calculate velocity induced currents $\vec{J}_0$ in a defect-free pipe wall due to axial motion of the magnetizer inside the pipe. (Step 1 Graphic)
- Step 2: Model an axial crack by applying a current $-\vec{J}_0\big|_i$ at the nodes *i* defining the crack and compute total perturbation current $\vec{J}_P$. (Step 2 Graphic)
- Step 3: Use results obtained in Step **2** to solve for the perturbation fields that can then be measured with an induction coil. Details associated with each step are provided below. (Step 3 Graphic)

Step 1. Calculation of Velocity Induced Currents

In the first step, a defect-free pipe with a magnetizer moving at a fixed velocity is modeled. The velocity induced current in the defect free pipe wall is calculated using the Leisman-Frind method. The axial distribution of currents on (1) the inner surface, (2) middle of pipe wall, and (3) outer surface of the pipe wall show that in the vicinity of the magnetizer, the current decays from the inside to the outside diameter of the pipe. The motion of the magnetizer at a fixed velocity, therefore, results in a current distribution that varies with each time step. The current is used as the source term in step 2, which models a section of the pipe wall in the remote field region. Details of Step 1.

Step 2. Calculation of Perturbation Current by the Presence of a Crack

In step 2, a tight crack of zero volume is introduced in the remote field region of the pipe. The basic assumption in this step is linearity of constitutive relations in the remote field region. That is, the total current in the presence of a crack is the sum of the background current in the defect-free pipe and the perturbation current introduced by the crack. Using this approach and ignoring the defect induced current term in the equation, we apply Neumann boundary conditions at the nodes to determine the perturbation currents to a first approximation. Details of Step 2.

Step 3. Calculation of Current Perturbation Fields

In the third step, the three-dimensional governing equation in terms of the vector magnetic potential is used to calculate the first approximation of the magnetic fields induced by the perturbation currents. This potential is then used to determine the defect-induced term that was ignored in the previous steps by iterating until convergence is obtained. The final solution is then used to calculate the associated flux density.

The motion of the tool is modeled by implementing steps 2 and 3 for each position of the defect relative to the inspection tool and the sensor coil. The induced voltage in sensor coil is then computed as a function of position. Details of Step 3.

Example

The inspection geometry used in the implementation of the finite-element model is shown below. Example of three-dimensional simulation of velocity-induced remote fields. This defect-free geometry is axisymmetric and, hence, a two-dimensional model was used in implementing step 1 to calculate the velocity-induced currents in each time step. In steps 2 and 3, the boxed section around the axial crack was modeled in three dimensions using the source currents obtained in step 1.

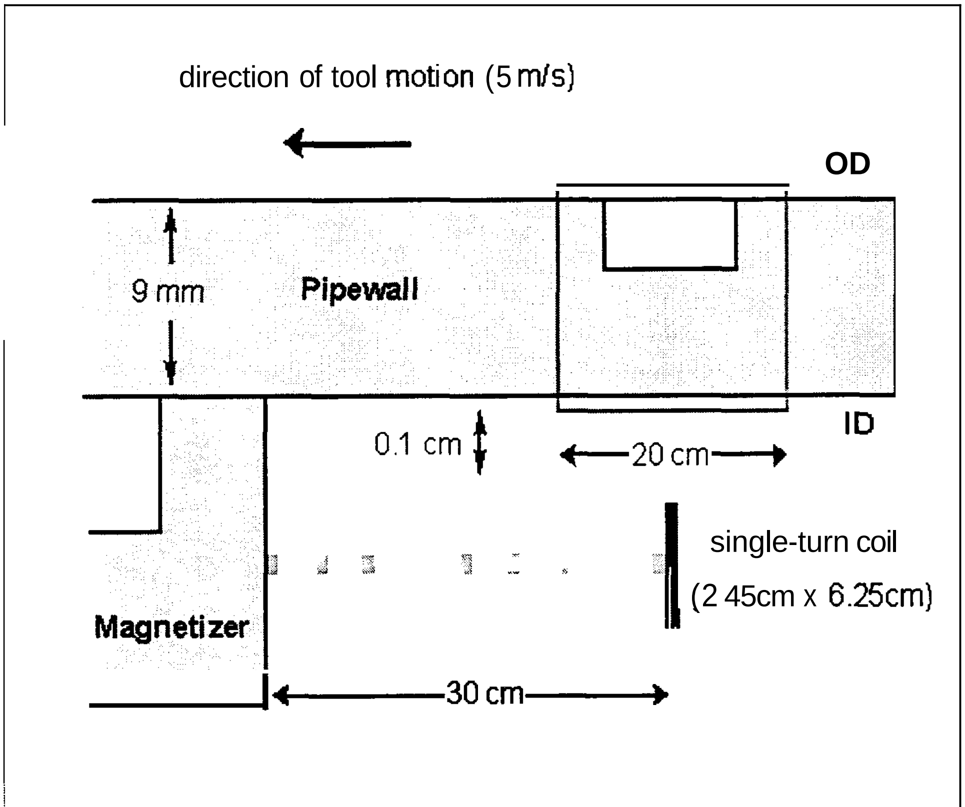

Example geometry

The resulting defect signals were calculated in terms of the voltage induced in a single turn coil by the axial component of the perturbation fields. The voltage signal as **a** function of the depth is shown below. The peak signals occur at the crack edges.

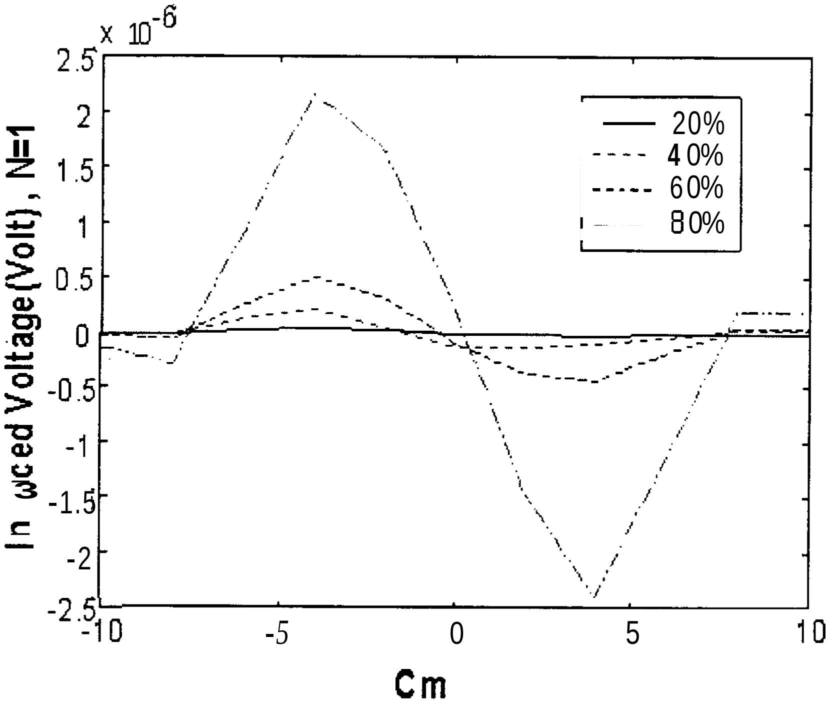

Induced voltage in a single turn coil
for different defect depths

Step 1 Graphic

- **Governing Equation:** $\nabla \times \frac{1}{\mu}\nabla \times \vec{A} = J_s - \sigma\frac{\partial A}{\partial t} + \sigma V \times \nabla \times \vec{A}$

  (*Leismann-Frind Method*)

- **Output: Velocity induced Current Distribution in defect free pipe** $(\vec{J}_0)$

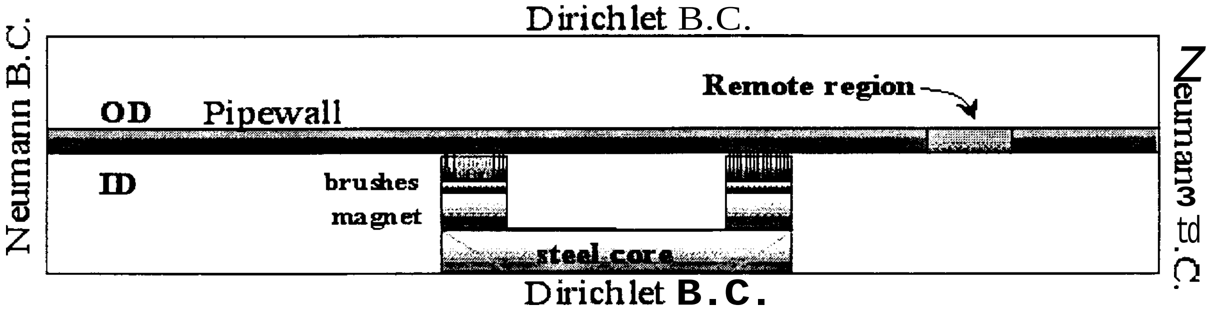

Step 2 Graphic

- **Governing equation:**

  $\nabla \cdot \sigma \nabla V = 0$

- **Input** : Current density $\vec{J}_0$ from **step 1**

- **Boundary condition:**

  $\frac{\partial V}{\partial n} = -\frac{\vec{J}_0}{\sigma}$ on SCC nodes

- **Output** : Perturbation current distribution $\vec{J}_p$

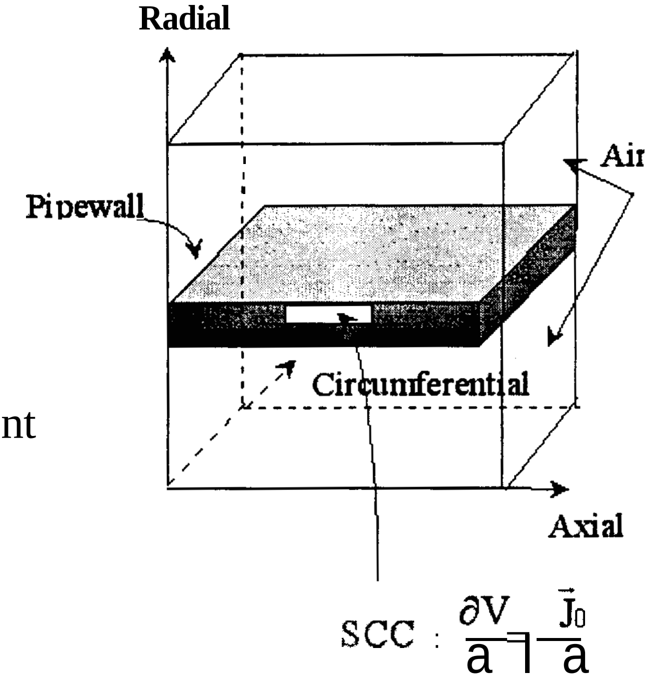

Step 3 Graphic

- **Governing equation:**

$$V \times \frac{1}{\mu} \nabla \times \vec{A} = \vec{J}_p$$

- **Input :** $\vec{J}_p$ from **step** 2

- **output :**

$$\vec{B} = \nabla \times \vec{A}$$

$$B_r, B_\theta, B_z$$

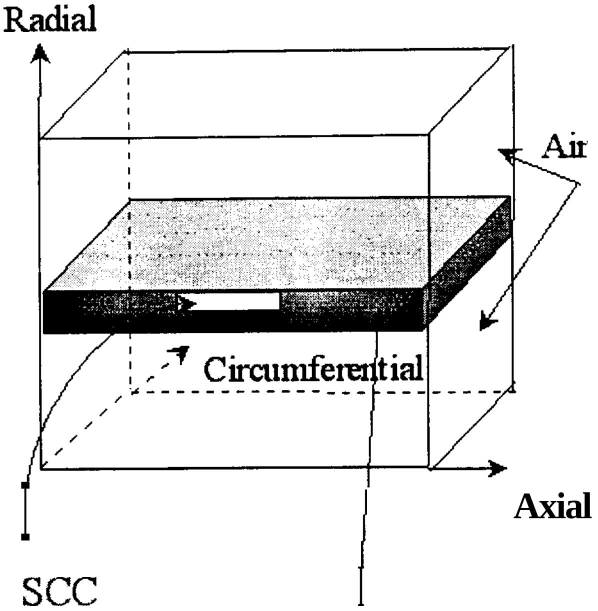

use the current density $\vec{J}_P$ from step 2 as a source

More Details on Finite-Element Modeling of Velocity-Induced Remote Fields

Details of Step 7

In the first step, a defect-free pipe with a magnetizer moving at a fixed velocity is modeled. The velocity induced current $\vec{J}_0$ in the defect-free pipe wall is calculated using the Leisman-Frind method:

$$\vec{J}_0 = -\sigma V \frac{\partial \vec{A}}{\partial z}$$

The motion induced current distribution in a defect-free pipe wall at a velocity of 5 m/s is shown below. The distribution of axial currents on (1) the inner surface, (2) middle of pipe wall, and outer (3) surface of the pipe wall show that in the vicinity of the magnetizer, the current decays from the inside to the outside diameter of the pipe. The motion of the magnetizer at a fixed velocity, therefore, results in a current distribution that varies with each time step. The current $-\vec{J}_0$ is used as the source term in step 2, which models a section of the pipe wall in the remote field region.

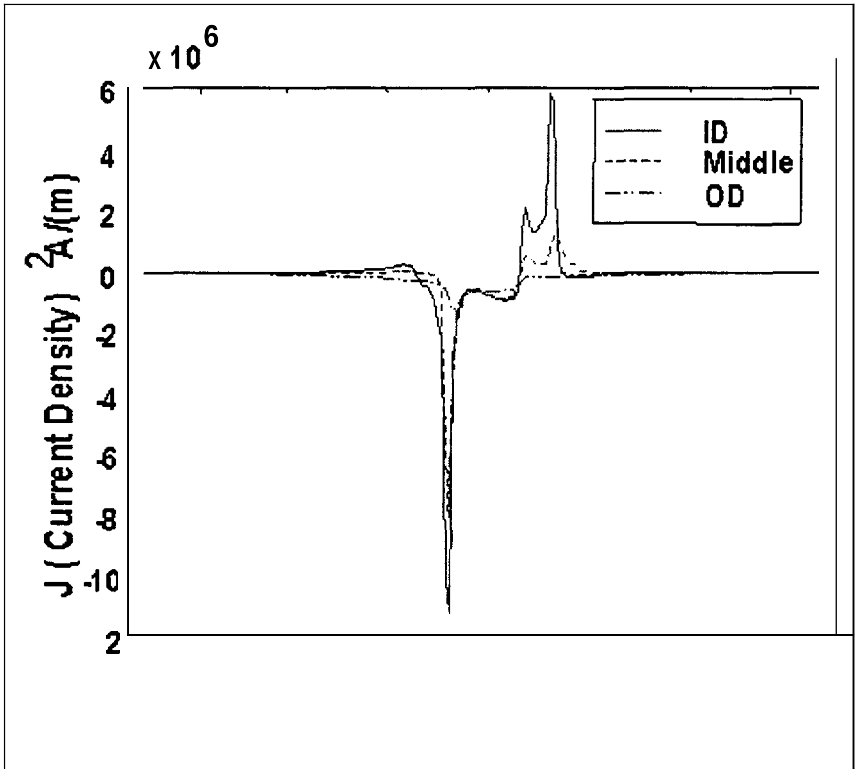

Motion induced current distribution
in pipe wall (velocity=5.0 m/s)

Details of *Step 2*

In the second step, a tight crack of zero volume Ω_{defect} is introduced in the remote field region of the pipe. The basic assumption in this step is linearity of constitutive relations in the remote field region. That is, the total current $\vec{J}$ in the presence of a crack is the sum of the background current $\vec{J}_0$ in the defect-free pipe and the perturbation anomalous current $\vec{J}_p$ introduced by the crack:

$$\vec{J}_p = \begin{cases} -\vec{J}_0 & \text{in } \Omega_{\text{defect}} \\ \text{unknown} & \text{in } \Omega^c_{\text{defect}} \end{cases}$$

where Ω^c_{defect} is the complement of Ω_{defect}. The total current is given by:

$$\vec{J} = \vec{J}_0 + \vec{J}_p$$

On Ω_{defect} we have

$$\vec{J}p = -\vec{J}_0 = \sigma(j\omega\vec{A} + \nabla V)$$

where V is the electric scalar potential.

Using this approach and ignoring defect induced currents, $j\omega\sigma\vec{A}$, we apply Neumann boundary conditions at the defect nodes *i*:

$$\frac{\partial V}{\partial n_i} = -\left.\frac{\vec{J}_0}{\sigma}\right|_i$$

The solution of the governing Laplace Equation $\nabla^2 V = 0$ gives to a first approximation, the perturbation currents $\vec{J}_p$ in the pipe wall section due to an axial crack.

Details of *Step 3*

In the third step, the three-dimensional governing equation in terms of the vector magnetic potential is used to calculate the first approximation of the magnetic fields induced by the perturbation currents. This potential is then used to determine the defect contribution to the current that was ignored in the previous step by iterating until convergence is obtained. The final solution is then used to calculate the associated flux density.

The governing equation for this step in terms of the vector magnetic potential is the three-dimensional equation

$$\nabla \times \frac{1}{\mu} \nabla \times \vec{A} = \vec{J}_p$$

where $\vec{J}_p$ is the current distribution obtained in step 2. The solution of this equation is the first approximation of $\vec{A}$. The solution is substituted in the earlier equation in the term $j\omega\sigma\vec{A}$ to correct the value of $\vec{J}_0$, and steps 2 and 3 are iterated until convergence is obtained. The final solution $\vec{A}$ is used for computing the associated flux density $\vec{B} = \nabla \times \vec{A}$

As an example, the axial component of the field (B) obtained in step 3 is plotted below. Note that the figure corresponds to the axial field component at one position of the magnetizer relative to the crack.

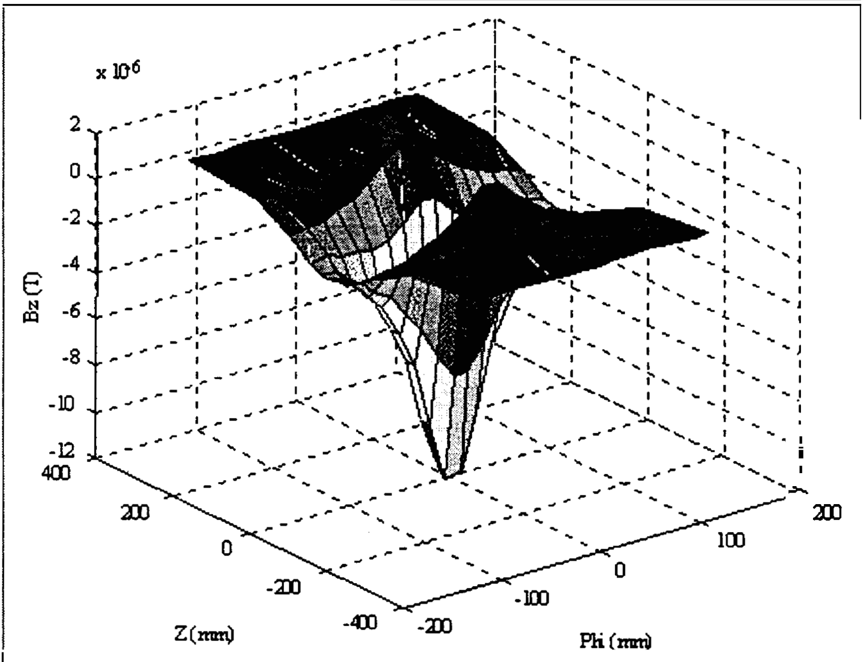

Axial component of magnetic field

The motion of the tool is modeled by implementing steps 2 and 3 for each position of the defect relative to the inspection tool and the sensor coil. This results in values ϕ_i of the total flux linking the coil at each position *j*. The induced voltage in sensor coil is then computed as a function of position:

$$V_i = -N\frac{d\phi_i}{dt}, i = 1,2,\cdots,n$$
$$= -N(\phi_i - \phi_i - 1)$$

where V_i is the signal due to axial component of current perturbation fields and N **is** number of turns of coil.

Example of Three-Dimensional Simulation of Velocity-Induced Remote Fields

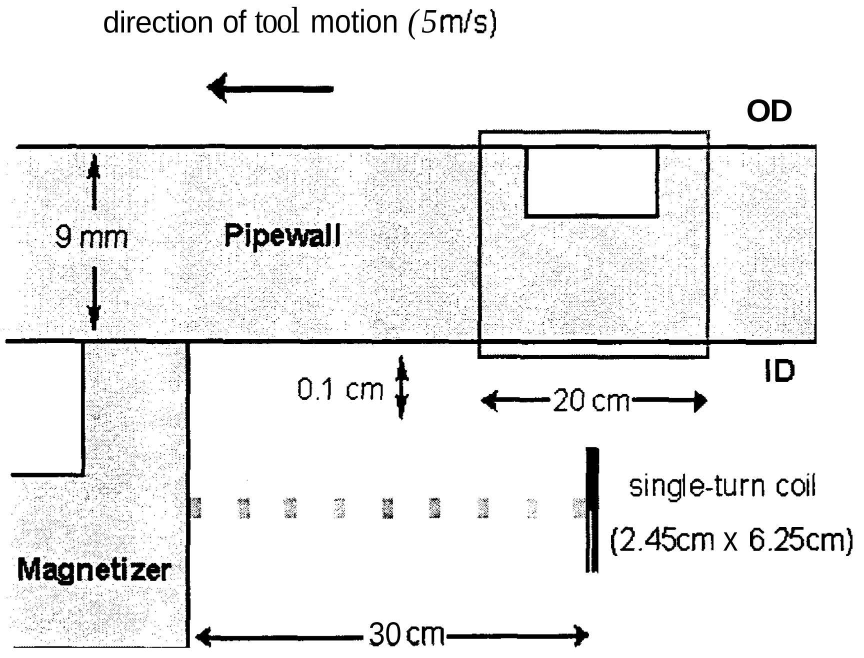

Example geometry

The voltage signal as a function of the depth of **a** crack whose length is 8 cm is shown below. The peaks occur at the crack edges.

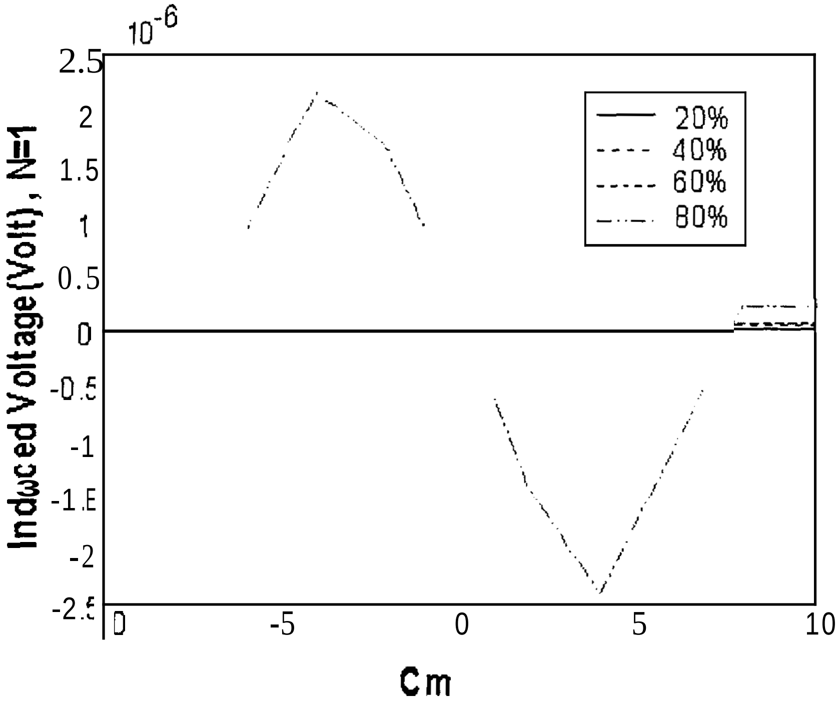

Induced voltage in a single-turn coil
for different defect depths

The peak-to-peak values plotted **as** a function of flaw depth show an exponential variation:

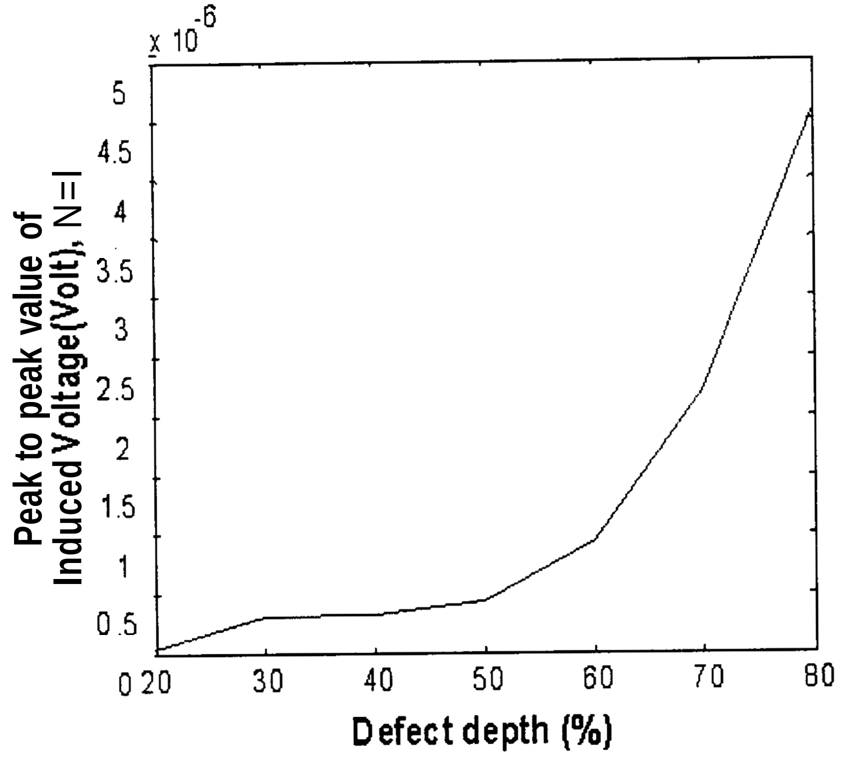

Peak-to-peak induced voltage in a single-turn coil as a function of defect depth

The signals obtained with various axial crack lengths are plotted below. The results show a monotonic increase in the peak value of the signal with defect length.

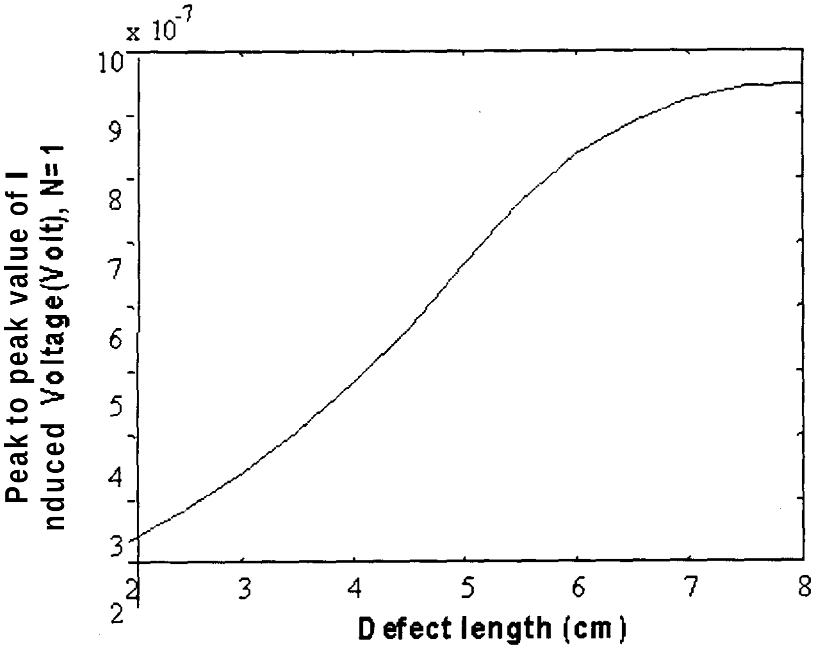

Peal

The signals shown in earlier were obtained when the coil axis was directly under the flaw. The signals obtained at other circumferential coil axis positions show a reduction in magnitude. The voltage signals at 0° , 7.9° , 15.8° , and 23.7° are plotted below. These signals show a reduction in the peak amplitude of the signal as the coil moves away from the crack.

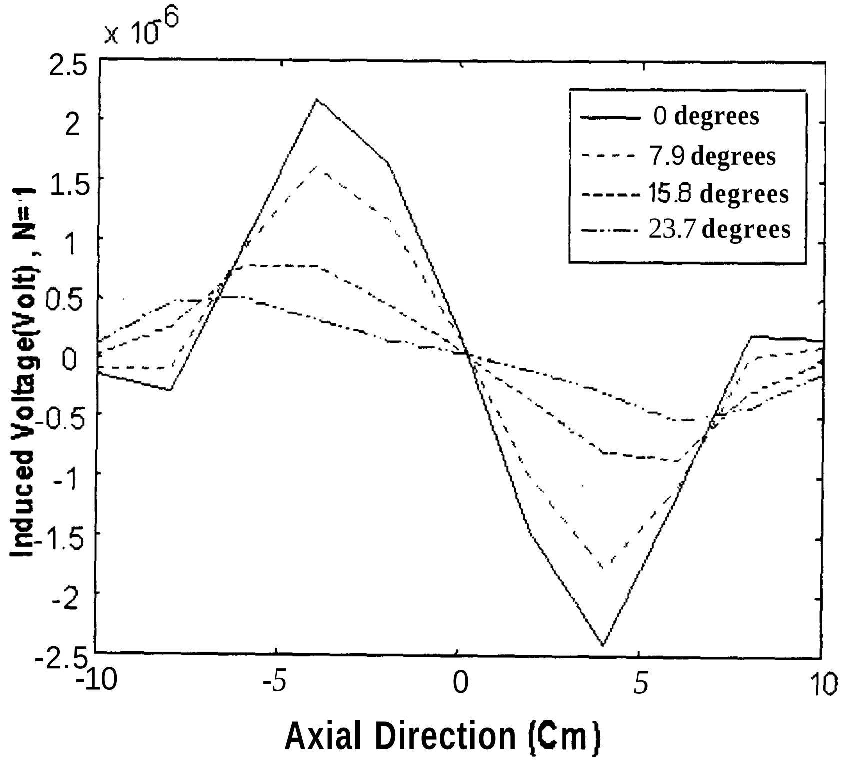

Induced voltage in a single-turn coil
as a function of circumferential position

Overview of Remote-Field Eddy-Current Techniques

In prior work for the Pipeline Research Committee, the remote-field eddy-current technique was successfully used to detect a variety of defects and material conditions in large-diameter pipeline steels. Limitations of this technique were also identified. In this project, we investigated methods to address these limitations by improving the sensitivity of the technique and increasing the inspection speed.

Traditional remote-field eddy-current techniques use low-frequency exciters, which limits the maximum speed at which inspection equipment can travel. Typically, these speeds have been less than one mile per hour, which severely limits the potential uses on in-line inspection equipment. Detecting SCC depends on the strengths of the eddy currents, which in turn, depend on the electrical conductivity and magnetic permeability of the pipe material.

A schematic of the remote-field eddy-current technique is shown below. An exciter, which is sized to nearly the same diameter as the inside diameter of the pipe, is driven with a low-frequency sinusoidal current. A small magnetic field sensor is positioned some distance away. One portion of the magnetic field generated by the exciter travels down the inside of the pipe, with the field directly coupled to the sensor. A second portion of the alternating magnetic field propagates through the material of the pipe, inducing eddy currents as it goes. Once the magnetic field penetrates the outside wall of the pipe, it spreads along the surface of the pipe and re-enters the pipe, again inducing eddy currents to flow in the pipe material. This second path is referred to as the remote path.

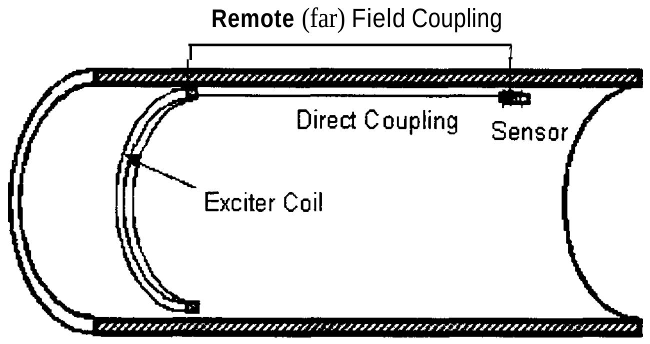

Remote-field eddy-current concept

The total magnetic field and eddy current flow at any point is the combination of directly coupled and remotely coupled fields. The key to remote-field eddy-current testing is to choose a sensor position where the remotely coupled field is large compared with a directly coupled field. This is possible because the directly coupled field decays at a faster rate.

Shown below is a semi-logarithmic plot of the decays of both the remote and direct field. Both decays are exponential and the decay constant for the direct field is nearly four times as fast as the remote field. Also, the combined magnetic field is less than the direct field in the near field, and it is less than the remote field in the far field. This phenomenon is due to the fact that phase difference for the two paths is always greater than 90 degrees for distances greater than a coil diameter.

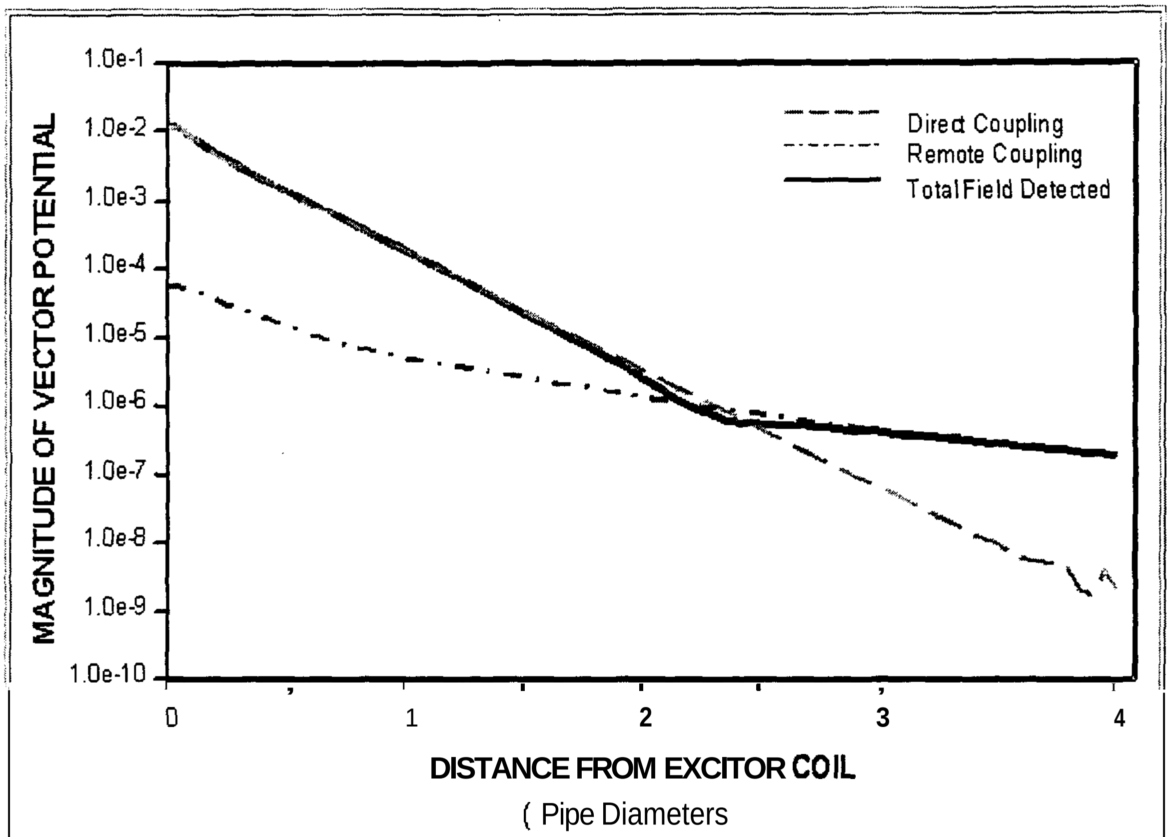

Relative signal strengths

At a distance from the exciter coil that is greater than about three pipe diameters, the remote field is larger than the direct couple field, and it constitutes the bulk of the total field. By placing a sensitive detector in this region, perturbations in the remote field as a result of axial cracks can be detected.

Details on Remote-Field Eddy-Current Experiments

Remote-field eddy-current techniques were investigated using the MFL test bed vehicle and various exciter coils and sensors. A sinusoidal current flowing in an exciter coil was used to induce currents in the pipe at various background magnetization levels. The test bed vehicle supplied the background fields needed to reduce the permeability of the pipeline steel.

Three critical experiments were performed to evaluate the improvements made to remote-field eddy-current results using magnetic saturation. They were used to

- Determine the placement of remote-field eddy-current exciter coil
- Detect stress corrosion cracks using exciter coil saturation
- Demonstrate noise reduction with magnetic saturation.

The results show that the relative permeability μ_r of the pipe can be reduced from 98 to 15 using magnetic saturation. This means the signal amplitude at the receiver should be nearly 6.5 times (> 98 / 15) greater with saturation than without.

Signal amplitude is proportional to the inverse of excitation frequency. The excitation frequency, in turn, limits the maximum inspection velocity: the higher the frequency, the higher the possible inspection speeds. By decreasing the relative permeability by a factor of 6.5, a 20-hertz signal through unsaturated pipe and 130-hertz signal through saturated pipe have the same signal level at the receiver. Hence, magnetic saturation could be used to help overcome implementation difficulties related to maximum inspection speed or signal amplitude.

The following figure shows a typical signal for a crack acquired at an excitation frequency of 100 Hertz. For this test, one sensor was rotated past the crack in the circumferential direction. Additional metal, in this case a 3/4-inch steel nut, was used to ensure the remote-field signal was being measured. As seen in the figure, the nut was placed next to the crack and subsequently on the crack. Placing the nut on the crack reduced the amplitude of the crack signal.

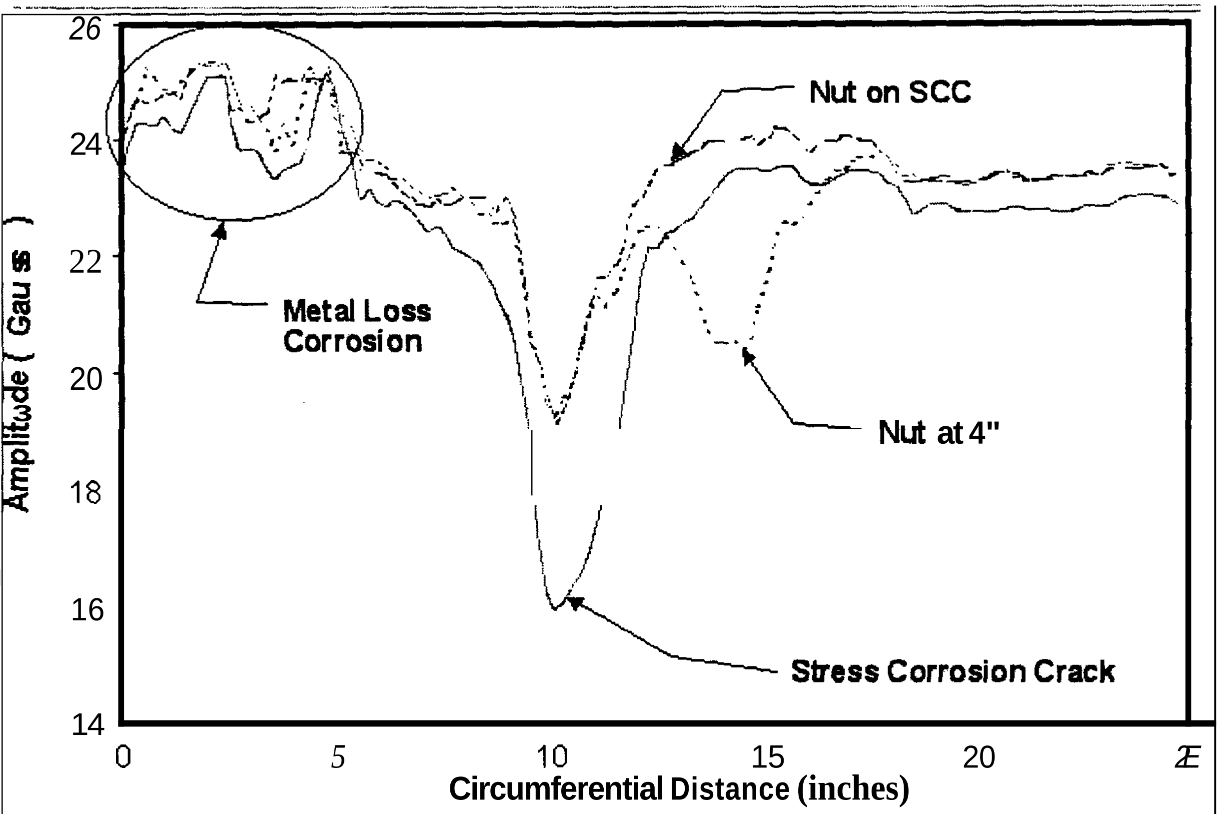

Remote-field eddy-current results

The signal levels at 100 Hertz were adequate for defect detection, but additional signal amplitude is always helpful. Since saturation at the exciter was useful, we expected that saturation at both the exciter and the receiver would provide even better signal levels. We attempted to verify this expectation as follows. The TBV magnetizer was used to provide magnetization at the exciter coil, and local magnetization was performed at the receiver coil by placing magnets on the outside of the pipe. Saturation at the exciter and receiver provided increased signal levels over the exciter saturation only, but the saturating field at the receiver was not uniform, and the drift in bias signal level masked the defect signals. Hence, the tests were not successful. Additional work is needed here.

An interesting result was observed when the receiver magnets were removed from the outside of the pipe, and the experiment was repeated with exciter saturation only. The noise levels were greatly increased in the regions where the magnets were placed and then removed. We hypothesize that the source of the noise was a randomization of the magnetic domains caused by the application and removal of the magnets. Consequently, aligning the magnetic domains by remagnetizing could reduce the background noise levels. To prove the potential this concept, the test bed vehicle was pulled through the test sample to realign the magnetic domains, and then the exciter saturation experiment was repeated. The signal and noise levels matched previous results, demonstrating the increase in noise due to randomized magnetic domains.

While the experiments with saturation at both the exciter and receiver coils were not successful because of equipment limitations, this technique should further increase the excitation frequency enabling. **Also,** the remote-field eddy-current technique with magnetic saturation has potential for detecting other defects in pipelines in addition to cracks.

Battelle

. . . *Putting Technology To* ***Work***

DTRS56-96-C-00 10

In-line inspection Technologies for Mechanical Damage
And SCC in Pipelines - Final Report

C-LINE #70568
CD **HOLDER**